Nonlinear Force-free Field Modeling of Solar Coronal Jets in Theoretical Configurations

Meyer, K. A.; Savcheva, A. S.; Mackay, D. H.; Deluca, E. E.

Published in:
Astrophysical Journal

DOI:
10.3847/1538-4357/ab271a

Publication date:
2019

Document Version
Publisher's PDF, also known as Version of record

The Astrophysical Journal, 880:62 (13pp), 2019 July 20 https://doi.org/10.3847/1538-4357/ab271a

Nonlinear Force-free Field Modeling of Solar Coronal Jets in Theoretical Configurations

K. A. Meyer[1], A. S. Savcheva[2], D. H. Mackay[3], and E. E. DeLuca[2]
[1] Division of Computing and Mathematics, Abertay University, Kydd Building, Bell Street, Dundee, DD1 1HG, UK; k.meyer@abertay.ac.uk
[2] Harvard-Smithsonian Center for Astrophysics, 60 Garden Street, Cambridge, MA 02138, USA
[3] School of Mathematics and Statistics, University of St Andrews, North Haugh, St Andrews, KY16 9SS, UK
Received 2017 March 17; revised 2019 April 24; accepted 2019 April 29; published 2019 July 25

Abstract

Coronal jets occur frequently on the Sun, and may contribute significantly to the solar wind. With the suite of instruments available now, we can observe these phenomena in greater detail than ever before. Modeling and simulations can assist further with understanding the dynamic processes involved, but previous studies tended to consider only one mechanism (e.g., emergence or rotation) for the origin of the jet. In this study we model a series of idealized archetypal jet configurations and follow the evolution of the coronal magnetic field. This is a step toward understanding these idealized situations before considering their observational counterparts. Several simple situations are set up for the evolution of the photospheric magnetic field: a single parasitic polarity rotating or moving in a circular path; as well as opposite polarity pairs involved in flyby (shearing), cancellation or emergence; all in the presence of a uniform, open background magnetic field. The coronal magnetic field is evolved in time using a magnetofrictional relaxation method. While magnetofriction cannot accurately reproduce the dynamics of an eruptive phase, the structure of the coronal magnetic field, as well as the buildup of electric currents and free magnetic energy are instructive. Certain configurations and motions produce a flux rope and allow the significant buildup of free energy, reminiscent of the progenitors of so-called blowout jets, whereas other, simpler configurations are more comparable to the standard jet model. The next stage is a comparison with observed coronal jet structures and their corresponding photospheric evolution.

Key words: Sun: activity – Sun: magnetic fields

Supporting material: animations

1. Introduction

Coronal jets are ubiquitous phenomena in the solar atmosphere. They have been observed at a range of wavelengths, from visible light (e.g., Wang et al. 1998) to EUV (e.g., Chen et al. 2008; Nisticò et al. 2009; Moore et al. 2013; Sterling et al. 2015) and X-rays (e.g., Savcheva et al. 2007; Shimojo & Tsuneta 2009; Sako et al. 2013). Jets are mostly known for their occurrence in coronal holes, where they appear as a consequence of the reconnection between a small-scale closed field structure and the open ambient field of the corona, forming the famous Eiffel tower shape (see the suggested cartoon by Shibata et al. 1996). They are also observed in active regions where the role of the large-scale field is played by long, over-arching active region loops. Most of the statistics of the observational characteristics of coronal jets (Savcheva et al. 2007; Sako et al. 2013; Sako 2014; Sterling et al. 2015) and the models and simulations that aim to explain these observations (Archontis & Hood 2008; Moreno-Insertis et al. 2008; Pariat et al. 2009, 2010; Archontis & Hood 2013; Moreno-Insertis & Galsgaard 2013; Fang et al. 2014; Pariat et al. 2015; Török et al. 2016; Karpen et al. 2017; Szente et al. 2017) are set in the context of coronal holes' open magnetic fields. Coronal jets have gained popularity because they are well observed with the increased spatiotemporal resolution of EUV and X-ray instruments like those on *Hinode*, *SDO*, and *IRIS*. In addition, it has been determined that coronal jets extend into the heliosphere (Bout et al. 2002), and because of their large frequency of occurrence, they may contribute significantly to the solar wind (Cirtain et al. 2007). Raouafi et al. (2016) provide a review of observations, theory, and modeling of coronal jets.

After the work of Moore et al. (2010, 2013) observations and modeling of coronal jets have been concentrated on the dichotomy of the standard versus blowout jet idea, which suggests the existence of two types of jets. Standard jets are pencil-like and hot, originating through simple reconnection processes like that in the Shibata et al. (1996) cartoon. Blowout jets are visually more complex, displaying a broad curtain-like spire, and originate from sheared and twisted bipole fields in something like a mini-filament eruption. Blowout jets also possess a cool counterpart in the observations. Nisticò et al. (2009) conducted a study of 79 jets, which they observed in EUV with *STEREO*. They divided these into three classifications: 37 were classified as Eiffel tower-type jets, 12 as lambda-type jets, 5 as microCME-type events, and 25 were unclassified. Moore et al. (2010) classed the combined 49 Eiffel tower and lambda-type jets of Nisticò et al. (2009) as standard jets, and the 5 microCME events as blowout jets. Moore et al. (2010) and Moore et al. (2013) found more of an even split between standard and blowout jets, with 53 being classified as standard and 50 as blowout across the 109 jets considered in the 2 studies (6 were unclassified). More recently, Sterling et al. (2015) suggested that all jets originate from mini-filament eruptions and that the difference depends on where the reconnection takes place with respect to the mini-filament, which points to the importance of twisted and sheared fields in the closed field part of the jet and how it is formed.

A variety of approaches have been taken in an effort to understand the mechanism(s) producing coronal jets: (A) purely observational case by case (Matsui et al. 2012) or statistical studies (Savcheva et al. 2007; Nisticò et al. 2009; Sako et al. 2013; Sterling et al. 2015); (B) (1) analytic models and cartoons (Shibata et al. 1996; Moore et al. 2010; Sterling et al. 2015); (2) zero-β MHD simulations of archetypal configurations (e.g.,

Pariat et al. 2009, 2010; Török et al. 2009); (3) non-zero β MHD simulations with additional physics of archetypal configurations, such as gravity or thermodynamics included (Archontis & Hood 2013; Moreno-Insertis & Galsgaard 2013; Fang et al. 2014; Pariat et al. 2015; Török et al. 2016; Karpen et al. 2017; Szente et al. 2017); and (4) data-driven magnetofrictional simulations (Cheung et al. 2015).

There is a long history of idealized MHD simulations of coronal jets in coronal and active regions' archetypal configurations—from the early 1990s to now, and more recently the jump to data-driven magnetofrictional simulations. Magnetofriction has successfully been used in data-driven simulations for the coronal magnetic field of active regions (Mackay et al. 2011; Cheung & DeRosa 2012; Gibb et al. 2014), active region jets (Cheung et al. 2015), and the small-scale magnetic field of the quiet Sun (Meyer et al. 2013). Magnetofriction is essentially a form of reduced MHD where there are no equations for the plasma (pressure, density etc.), only the induction equation for the magnetic field and the corresponding equations for electric fields, currents, and velocities. As such it is much less computationally intensive to run and a range of magnetic field configurations of coronal jets can be explored with ease.

One drawback of the above suite of abundant MHD simulations is that most of them essentially explore one mechanism for the formation of the jet's magnetic field prior to eruption, although they differ to various extents on the details of the triggers and drivers of the eruption itself, i.e., that is most of them assume the jet is formed by flux emergence, with the exception of Pariat et al. (2009, 2010, 2015) and more recently, Karpen et al. (2017) and Szente et al. (2017), who assumed a twisting of the base of the jet. Very few studies have looked at the photospheric magnetic flux evolution of coronal jets before and during their formation, and those that do are mainly case studies (Hong et al. 2011; Adams et al. 2014; Young & Muglach 2014a, 2014b; Panesar et al. 2016). All these studies report conclusively on the occurrence of flux cancellation between opposite polarities at the formation of the jet, but no study has yet reported a magnetic field observation of flux emergence at a jet onset. There are few statistical studies on the matter, partly because most attention has been concentrated on jets in polar coronal holes where the magnetic fields are not observed well. Clearly the situation can be remedied by a systematic statistical study. Shimojo & Tsuneta (2009) considered the correlation between SOT and XRT fields and jets. The dynamics of the magnetic field cannot be followed, as SOT-SP is rastering, but the high spatial resolution and sensitivity allow for magnetic field measurements near the pole. Panesar et al. (2016) studied 10 on-disk observations of coronal jets using AIA and HMI. They found that in all 10 cases, magnetic flux cancellation was occurring on the photosphere beneath the jet in the lead-up to its eruption. Innes et al. (2016) carried out a review of jet studies. In 12 of the 30 cases they considered, flux cancellation was observed to occur below the jet.

Because recent studies suggest that flux emergence may not be the main mechanism for jet formation, we were further prompted by the unique opportunity to realize a range of jet configurations with little computational cost using magnetofrictional evolution. The structure of the paper is as follows. Section 2 presents the magnetofrictional model and the setup of each jet configuration considered. Section 3 presents results, and Section 4 provides the discussion and conclusions.

2. Model

Inspired by recent observations of coronal jets in coronal holes and active regions, as well as the suite of MHD simulations, we set up magnetofrictional simulations of several basic configurations shown to produce coronal jets. Although magnetofrictional simulations have not been used for this purpose before, and they cannot accurately model the dynamics of the eruptive phase of the jet as well as MHD, we believe that these simulations are warranted as they are much less computationally expensive than an MHD simulation, and the basic behavior of the magnetic field and current is instructive. By performing this kind of modeling, we build a primer of sorts for different jet configurations and "dynamics," governed by the behavior of the photospheric magnetic field. Each simulation is composed of a 2D time-evolving photospheric magnetic field, described in Section 2.2, which is the lower boundary condition driving the continuous evolution of the 3D coronal magnetic field (Section 2.1).

2.1. Coronal Model

To model the coronal magnetic field, we use a technique called *magnetofriction* that is based on the method of van Ballegooijen et al. (2000). The corona is evolved continuously through a series of nonlinear force-free (NLFF) equilibria in response to an evolving photospheric boundary condition. A strength of this technique is that the coronal magnetic field retains a "memory" of the magnetic field connectivity, so that we may follow the buildup of current systems and free magnetic energy. This is in contrast to many other NLFF field modeling techniques, that produce independent extrapolations of the coronal field at each time (e.g., techniques discussed in Schrijver et al. 2006). This allows us to model a large range of different scenarios and explore the parameter space. Since magnetofriction considers equilibria, we cannot properly model the eruptive phase of the jet's evolution, but we can follow the evolution of its magnetic field structure, and the buildup and location of electric currents and free magnetic energy up until that point.

For each simulation, the computational domain is open at the top, to allow for flux-imbalance at the photosphere. The domain is closed in the y-direction, but periodic in the x-direction, to allow for an inclined uniform background magnetic field. In all simulations with an inclined background field, the inclination is in the positive x-direction. This background magnetic field represents a coronal hole or other predominantly unipolar region where jets are often observed, such as a parasitic polarity in the outskirts of a large active region.

The coronal field is evolved via the ideal induction equation

$$\frac{\partial \boldsymbol{A}}{\partial t} = \boldsymbol{v} \times \boldsymbol{B}, \tag{1}$$

where $\boldsymbol{A}$ is the vector potential, $\boldsymbol{B} = \nabla \times \boldsymbol{A}$, and $\boldsymbol{v}$ is the magnetofrictional velocity

$$\boldsymbol{v} = \frac{1}{\nu}\frac{\boldsymbol{j} \times \boldsymbol{B}}{B^2}, \tag{2}$$

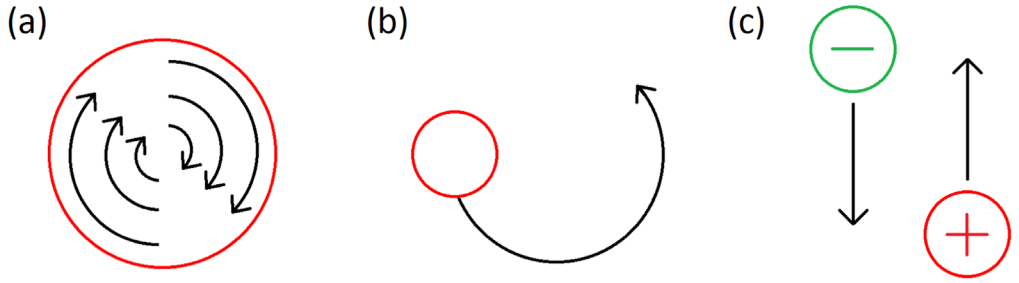

Figure 1. Three of the photospheric setups for this study: (a) a positive polarity with approximately solid-body rotation; (b) a positive polarity moving in a circle; (c) flyby.

following Yang et al. (1986), with ν being the coefficient of friction. The initial condition for each of our simulations is a potential magnetic field extrapolated from the first frame of the synthetic magnetogram series that composes our evolving photospheric boundary condition (see Section 2.2). Each subsequent frame in the series then provides footpoint motions at the base, that perturb the coronal field out of equilibrium, resulting in $\boldsymbol{j} \times \boldsymbol{B} \neq 0$. The magnetofrictional velocity then acts in the direction of the Lorentz force to relax the field back toward an equilibrium state. For the simulations described here, we take 1000 relaxation steps between synthetic magnetogram frames.

2.2. Photospheric Model

We require only the normal component of the magnetic field (B_z) at the photosphere. Each magnetic feature within the photospheric model is assumed either to have a simple Gaussian form

$$B_z = B_0 e^{-r^2/r_0^2}, \tag{3}$$

where $B_0 = 88$ G is the peak strength, r_0 is the Gaussian half-width, and r is the distance from the center of the feature; or have the same form as Pariat et al. (2009, 2010) (described below). At each time step, we move the central point (x, y) of each magnetic feature and analytically specify its B_z profile, rather than advecting B_z numerically. This avoids certain undesirable numerical effects such as diffusion or overshoot from differentiating numerically, which can propagate errors into the coronal volume. The synthetic magnetograms for the photospheric boundary are composed of the magnetic feature B_z profile(s) plus a uniform background magnetic field contribution. Because the coronal field induction Equation (1) is specified in terms of the vector potential, $\boldsymbol{A}$, we compute the A_x and A_y corresponding to B_z on the photosphere to use as our lower boundary condition (see Meyer et al. 2012). Each simulation has a grid size of 256×256 in the x and y directions. The rotating and circular motion simulations also have 256 grid cells in the z direction, while the emergence, cancellation and flyby have 150 grid cells in the z direction. Each magnetic feature in the simulations described below has a minimum of 20 grid cells across its diameter.

2.2.1. Rotation

We consider five main setups in this study, illustrated in Figures 1 and 2. The first setup (Figure 1(a)) is similar to that of Pariat et al. (2009, 2010). We include a single positive magnetic feature in a uniform negative background magnetic field, in a 18×18 Mm box. The background magnetic field is of strength -1 G and is either vertical (as in Pariat et al. 2009) or inclined at 10° to the z-axis (as in Pariat et al. 2010). We will denote these two simulations "PAD09" and "PAD10," respectively. The positive feature is given the same B_z profile as that of Pariat et al. (2009, 2010):

$$B_z(x, y, z) = \frac{\mu_0 m_0}{4\pi} \frac{2(z - z_0)^2 - (x - x_0)^2 - (y - y_0)^2}{((x - x_0)^2 + (y - y_0)^2 + (z - z_0)^2)^{5/2}} - B_v \cos\theta, \tag{4}$$

where $\mu_0 m_0 / 4\pi = 25$, $(x_0, y_0, z_0) = (9, 9, -1.5)$ Mm, $B_v = 1$ G is the strength of the background field and θ is the inclination of the background field with respect to the z-axis. The velocity profile for the rotation of the positive feature is given by

$$\boldsymbol{v}_\perp = v_0 k_B \frac{B_r - B_l}{B_z} \tan\left(k_B \frac{B_z - B_l}{B_r - B_l}\right) \boldsymbol{z} \times \nabla B_z, \tag{5}$$

following Pariat et al. (2009), where $k_B = 15$, v_0 is the magnitude of the twisting motions and $B_z \in [B_l, B_r]$. As in Pariat et al. (2009), we set $B_l = 0.1$ G and $B_r = 13$ G so that only the positive polarity flux is rotated, but while they multiply $\boldsymbol{v}_\perp$ by a time-dependent scalar $f(t)$ to gradually accelerate and decelerate the rotation, we set $\boldsymbol{v}_\perp$ to be constant in time. This velocity profile results in approximately solid-body rotation of the positive feature, where one full rotation takes approximately 50 time steps. The radius of the positive polarity is 1.5 Mm, which means that a point on its circumference moves approximately 0.188 Mm (7.2°) per time step. However, 1000 intermediate steps are taken between each magnetogram "time step" during the coronal evolution, so that the maximum distance a point on the circumference moves is 1.88×10^{-4} Mm, which is much less than the grid resolution, $\Delta x = 0.07$ Mm. This corresponds to the maximum movement that a footpoint of a magnetic field line can make between coronal relaxation steps. During each intermediate iteration, we allow five magnetofrictional relaxation steps between footpoint motions (i.e., 5000 magnetofrictional steps between magnetograms altogether). Five steps was determined to be optimal for achieving a relaxed solution and for propagation of information into the computational domain, without significantly increasing computational time. An additional simulation is also run, where we stop the photospheric driving in PAD09 at the time we see

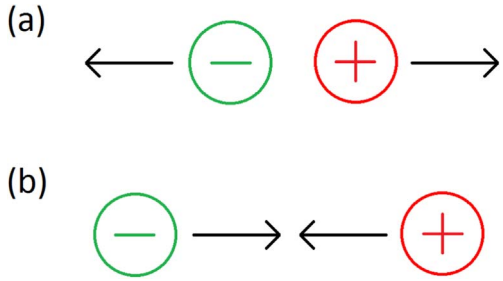

Figure 2. Two of the photospheric setups for this study: (a) emergence and (b) cancellation.

the onset of the kink instability, and allow the magnetic field to relax. This simulation is denoted "PAD09R."

2.2.2. Circular Motion

The second setup that we consider (Figure 1(b)) is a single positive magnetic feature moving in a circle of radius 1 Mm about the midpoint of the 30×30 Mm computational domain. The feature completes one lap every 50 time steps. For the simulation presented here, the feature is given the same B_z profile as above (Equation (4)) analytically specified at each time step from the feature's new (x, y) coordinates, and we include a constant background magnetic field of strength -1 G, inclined at 10° to the z-axis. We denote this simulation "CIRC." The justification for such a setup are observations of arc-like or swirling motions in the photosphere and chromosphere (e.g., Wedemeyer-Böhm & Rouppe van der Voort 2009; Wedemeyer-Böhm et al. 2012; Morton et al. 2013). Since the positive polarity has a radius of 1.5 Mm (as above), the maximum distance that a point on its circumference will move during a time step is $2\pi(1+1.5)/50 \approx 0.314$ Mm. The maximum distance moved during the coronal evolution (1000 relaxation steps) is therefore 3.14×10^{-4} Mm, which is much less than the grid resolution of $\Delta x = 0.117$ Mm.

For both the first and second setups, we also considered simulations where the positive feature had a Gaussian profile, as well as different strengths and inclinations of the uniform background field, but the results were not significantly different and will be mentioned only in passing in Section 3.

2.2.3. Flyby

The third setup that we consider is a "flyby" (Figure 1(c), e.g., Galsgaard et al. 2000; Meyer et al. 2012), in which a positive and negative magnetic feature are moved past one another in a 30×30 Mm computational domain, never interacting at the photospheric level. The midpoints of the features are 3 Mm apart at their closest point, halfway through the simulation. Here the features are given Gaussian profiles in B_z and again have a constant, 10° inclined background magnetic field of strength -1 G. Two flyby cases are considered. In the first, "FLYBY1," the setup illustrated by Figure 1(c) is rotated anti-clockwise by 90° so that the positive (negative) feature moves in the negative (positive) x-direction and the features pass one another at the mid-line $x = 15$ Mm. In the second case, "FLYBY2," the features move past one another in the y-direction, passing one another at the mid-line $y = 15$ Mm. As illustrated by Figure 1(c), the positive (negative) feature moves in the positive (negative) y-direction. The features move 5 Mm in total during each simulation of length 50 time steps.

2.2.4. Emergence and Cancellation

The final two setups that we consider are an emergence and cancellation (e.g., Meyer et al. 2012) in a 30×30 Mm computational domain, illustrated by Figures 2(a) and (b) respectively. In the emergence case, two Gaussian magnetic features of equal and opposite flux initially fully overlap at the center of the box, such that their net flux is zero. As the simulation progresses, the features are moved apart in the x-direction. This causes their Gaussian profiles to grow in flux as they separate, simulating emergence. The features move to 3 Mm apart over 30 time steps, then remain stationary for 30 time steps. The cancellation is almost exactly the opposite of the emergence. Two Gaussian features of equal and opposite flux are initially 3 Mm apart in the x-direction. They move together until they fully overlap at the center of the box after 30 time steps, hence their net flux becomes zero. The simulation is allowed to run for a further 30 time steps after full cancellation has occurred. In both simulations, there is a constant, 10° inclined background magnetic field of strength -1 G.

2.3. Initial Condition

Once the photospheric boundary condition has been set up as a series of synthetic magnetograms, we compute the initial condition for each simulation as a potential field extrapolation from the first photospheric boundary frame. Subsequent evolution is determined by the magnetofrictional relaxation technique described in Section 2.1. For all simulations, a magnetic null point is present in the corona, with a separatrix surface separating the positive polarity from the negative uniform background field (and the negative polarity in the cases involving a bipole).

3. Results

We discuss each of the simulations described in Section 2 in turn. For all simulations we specifically focus on the buildup of free magnetic energy, currents, and twist, as well as the motion of the magnetic null point.

3.1. PAD09, PAD10, and PAD09R

Figures 3(a) and (b) show field line plots in the xz-plane from the (a) PAD09 and (b) PAD10 simulations at $t = 30$ (left), $t = 70$ (center) and $t = 200$ (right) time steps, after 0.6, 1.4, and 4 rotations, respectively. A representative selection of magnetic field lines have been plotted to show the closed field within the dome (magenta) and background open field (blue). This can also be seen in the animation online. The red/green contours in the animation show the line-of-sight component of the current. In both simulations, the structure is of a dome (or fan) separatrix surface enclosing the positive polarity, with a magnetic null point connecting the dome to a vertical (PAD09) or inclined (PAD10) axis. As the positive polarity is rotated, the magnetic field within the dome becomes twisted. This causes magnetic energy within the dome to increase, and the dome to expand and rise.

Considering first the PAD09 simulation, the evolution is very similar to the models of Pariat et al. (2009) and Rachmeler et al. (2010). We see a continual rise and expansion of the jet dome until the system begins to kink. The onset of the kink begins around $t = 50$ time steps. This can be seen in Figure 4(a) (black line), which shows the height of the magnetic null point as a

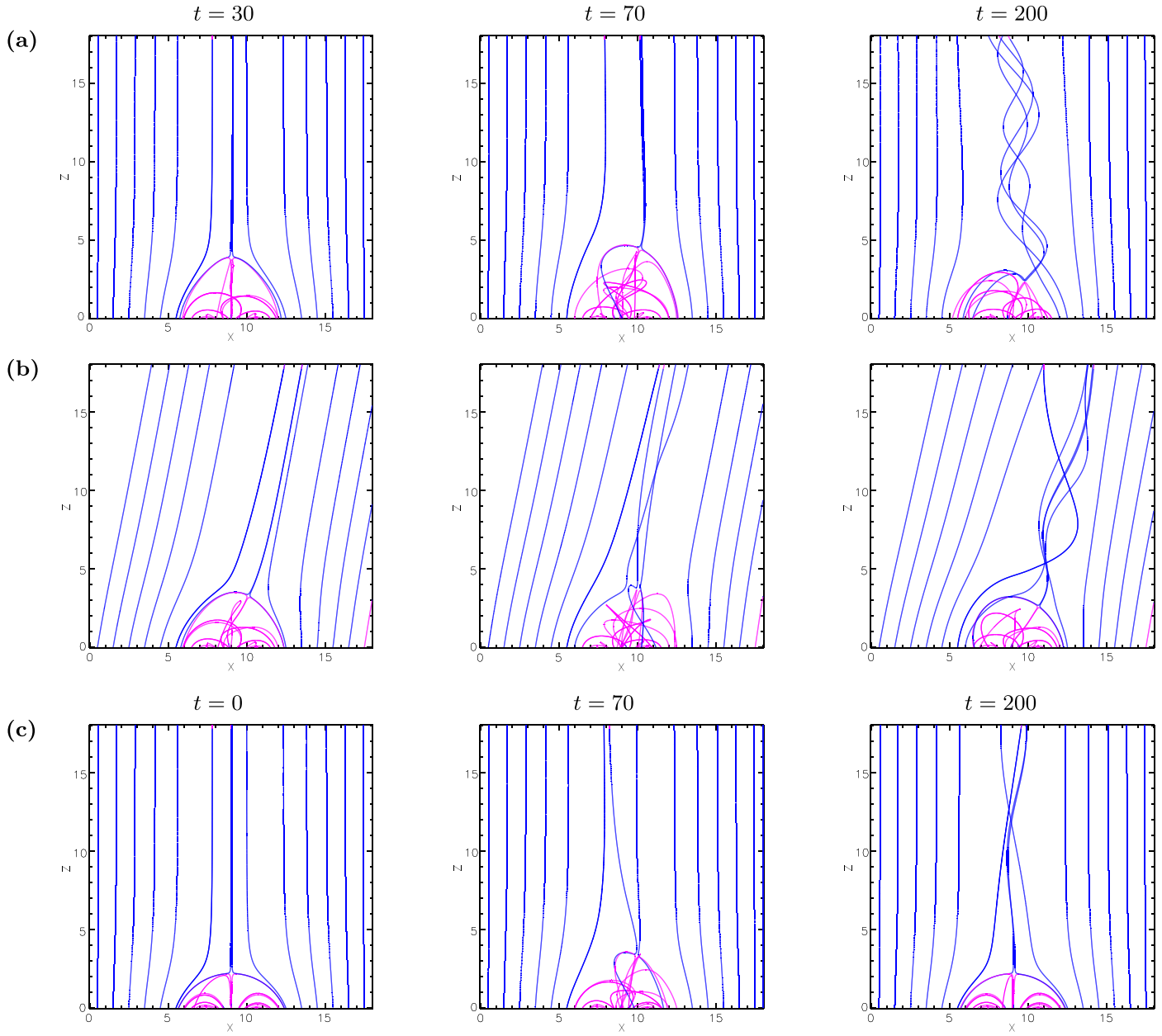

Figure 3. Closed (magenta) and open (blue) magnetic field lines viewed in the *xz*-plane at $y = 9$ Mm, for (a) PAD09, (b) PAD10, and (c) PAD09R. For (a) and (b), plots are shown at $t = 30$ time steps (left, 0.6 rotations), $t = 70$ (center, 1.4 rotations—after onset of kink), and $t = 200$ (right, 4 rotations). For (c), PAD09R, plots are shown at $t = 0$ time steps (left), $t = 70$ (center), and $t = 200$ (right). Note that PAD09 and PAD09R are identical at $t = 0$ and $t = 30$ time steps, so plot (a) left and (c) left apply to both simulations. An animation of the *xz*-plane at $y = 9$ Mm for the (a) PAD09, (b) PAD10, and (c) PAD09R simulations from time step 0 to 200 is provided online.

(An animation of this figure is available.)

function of time. Initially, the null steadily increases in height as the jet dome expands. Once the kink occurs around $t = 50$ time steps, the symmetry of the system is broken and the jet dome begins to tip over. This also allows for changes in connectivity or "reconnection" to occur, similar to Pariat et al. (2009). In Rachmeler et al. (2010), the axis also kinks, but their FLUX code models an ideal evolution, thus it does not allow for reconnection and there is no eruption. Since our code follows an ideal evolution, and cannot accurately simulate reconnection, we refer instead to "changing connectivity" when discussing our magnetofrictional simulations. This changing connectivity is a result of numerical diffusion, which is unavoidable in any finite difference numerical model, but is much less than what would result from including an explicit, non-ideal diffusion effect (such as in Pariat et al. 2009). This also means that the magnetofrictional model cannot accurately simulate the dynamic and rapid energy release of an eruptive event or instability; it can, however, follow the buildup of energy within the simulation up to the point at which the instability forms. Figure 4(b) (black line) shows the free magnetic energy as a function of time for the PAD09 simulation. We do see a drop in the free magnetic energy after the kink instability occurs, with the initial peak in free magnetic energy occurring around $t = 70$. This release of energy takes longer to onset than in the simulation of Pariat et al. (2009) due to the quasi-static nature of the magnetofrictional method.

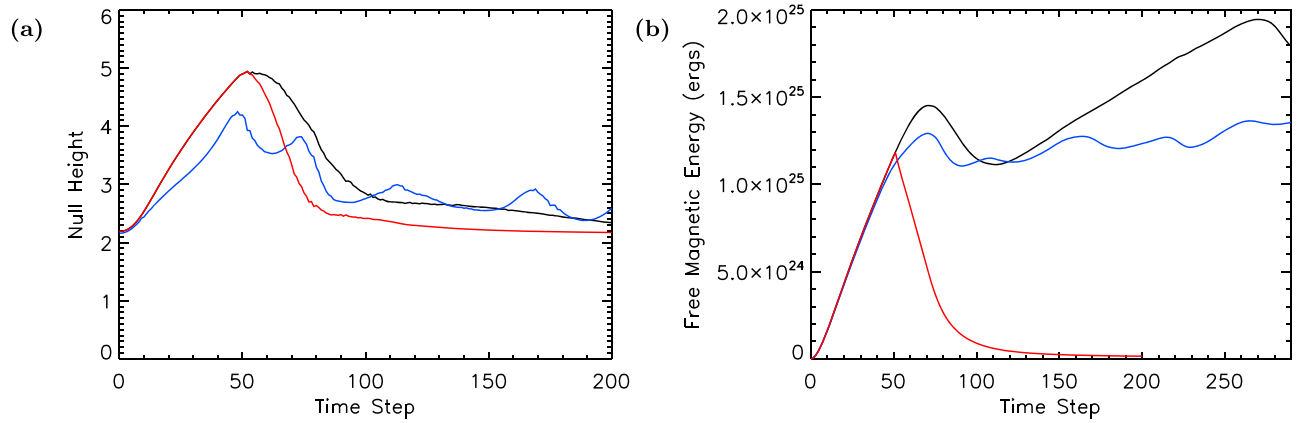

Figure 4. (a) Height of magnetic null point and (b) free magnetic energy as a function of time for PAD09 (black), PAD10 (blue), and PAD09R (red).

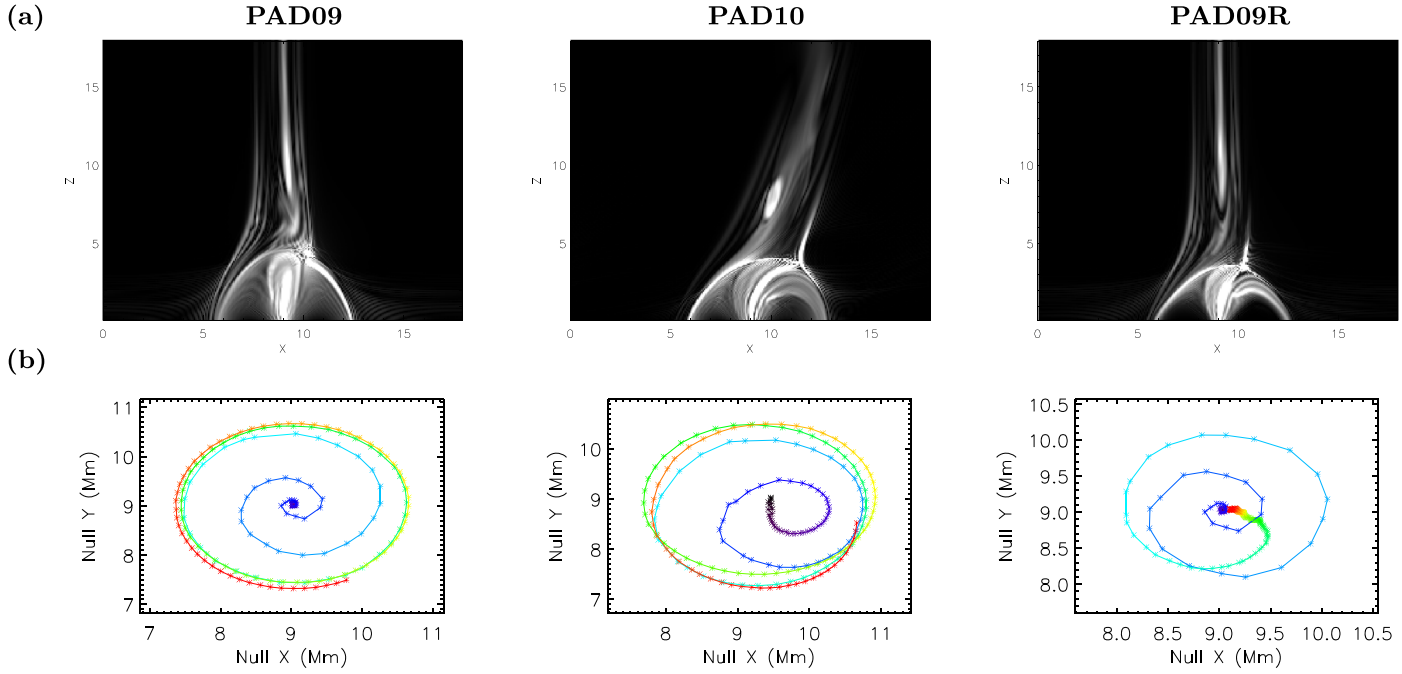

Figure 5. Plots for PAD09 (left), PAD10 (center) and PAD09R (right). (a) $|j|/|B|$, viewed in the xz-plane at $y = 15$ Mm, at $t = 70$ time steps (1.4 rotations). (b) xy path of magnetic null point in time from $t = 0$ (black) to $t = 200$ (red) time steps. An animation of $|j|/|B|$ in the xz-plane at $y = 15$ Mm for the PAD09, PAD10 and PAD09 simulations from time step 0 to 200 is provided online.

(An animation of this figure is available.)

We continue to drive the photospheric boundary with a constant velocity throughout the simulation. The result is that, after the first release of energy, the free energy begins to steadily increase again. The continual driving prevents the magnetic field from relaxing back toward an axisymmetric state. This means that magnetic connectivity can now change more readily, continually releasing energy, so this phase of free energy increase is more gradual than in the initial phase. Eventually, a second peak occurs after 270 time steps (5.4 rotations).

An additional simulation, PAD09R, is run with the same initial setup and photospheric driving velocity as PAD09, but we stop the driving after $t = 50$ time steps, as this is the time that we see the onset of the kink. The magnetic field is then allowed to relax for the remainder of the simulation. Figure 3(c) shows field line plots in the xz-plane for PAD09R at $t = 0$ (left), $t = 70$ (center), and $t = 200$ (right) time steps. The evolution can also be seen in the animated Figure 3. The magnetic field of PAD09R from $t = 0$ to $t = 50$ is identical to that of PAD09 (this means that Figure 3(c), left, shows field lines at $t = 0$ for both PAD09 and PAD09R; and Figure 3(a), left, shows field lines at $t = 30$ for both PAD09 and PAD09R). The snapshot at $t = 70$ shows field lines from PAD09R just after the kink has occurred, so it can be seen that the magnetic structure is tilted. By $t = 200$, the magnetic field has relaxed back to a position similar to its initial potential field position (compare with the Figure 3(a) right hand plot from PAD09, where the magnetic structure is still tilted and the field is extremely twisted due to continual photospheric driving). It takes a while for the null point to return to its equilibrium position in the PAD09R simulation. During the time that the magnetic structure is still non-symmetric, magnetic

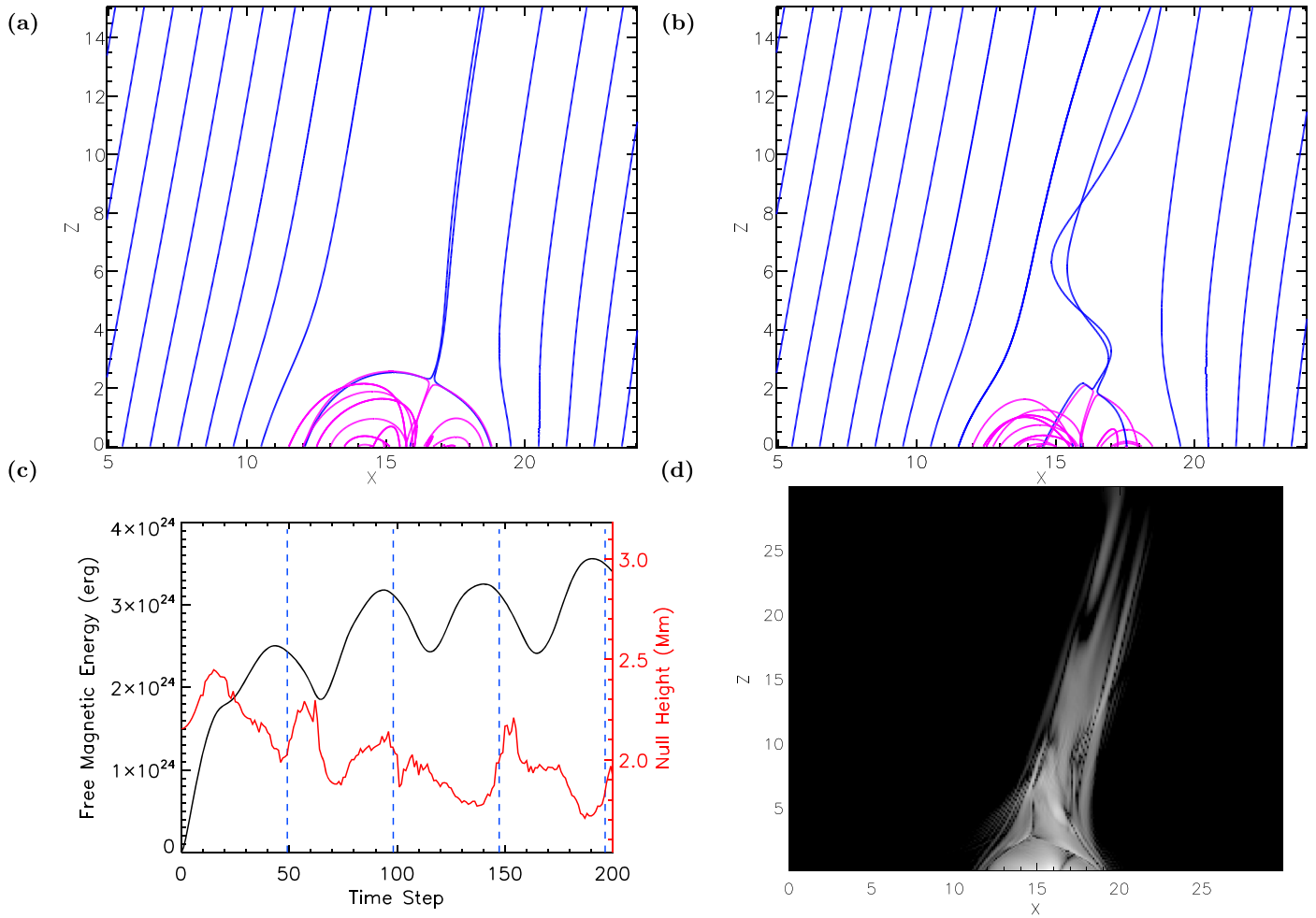

Figure 6. CIRC: (a) and (b) magnetic field lines (closed, magenta; open, blue) viewed in the *xz*-plane at $y = 9$ Mm, at $t = 30$ (0.6 rotations) and $t = 120$ time steps (2.4 rotations). (c) Free magnetic energy (black) and height of null point (red) as a function of time. (d) Logarithm of current, viewed in the *xz*-plane at $y = 15$ Mm, at $t = 120$ time steps (2.4 rotations). An animation of the magnetic field lines viewed in the *xz*-plane at $y = 9$ Mm (left panel) and the logarithm of the current, viewed in the *xz*-plane at $y = 15$ Mm (right panel) evolving from time step 0 to 200 are provided online.

(An animation of this figure is available.)

connectivity can still change readily, which transfers twist and free energy from the jet dome to the open field. This twist and energy is then propagated out through the open top boundary. By $t = 200$, the field is still slightly non-potential, with some free energy within the closed loops and along the twisted open field lines. The plots of null height (Figure 4(a), red line) and free magnetic energy (Figure 4(b), red line) also indicate that the system has almost relaxed back to its equilibrium state. The free magnetic energy (b) sharply drops as soon as the photospheric driving stops. This is because energy is being propagated out of the open top boundary along the jet spire, but is no longer being injected through the lower boundary. The null height (a) continues to increase until around $t = 70$, showing that the jet dome has continued to expand. The decrease in null height after this point is more rapid than that in PAD09 (black line) as there is no longer photospheric driving injecting energy and twist into the field.

We now compare our PAD10 simulation with that of Pariat et al. (2010), as well as PAD09 and PAD09R. In Pariat et al. (2009) they see a peak and sudden drop in free magnetic energy when the eruption occurs after kinking breaks the symmetry of the model. In Pariat et al. (2010), the model is initially set up to be non-symmetric, with the background magnetic field inclined at 10° to the vertical. They continue to rotate the positive magnetic polarity after the first eruption, resulting in a series of eruptive events, hence a series of peaks and drops in free energy. The free magnetic energy in our model can be seen in Figure 4(b) (blue line). We do see a series of peaks in our model, but they are not sharply defined, as there is not as rapid a decrease in energy after each peak. Again, this is due to the quasi-static nature of the magnetofrictional method. We cannot accurately follow the dynamics of an eruption, so the result is that not as much energy and twist is released before it starts building up again due to the photospheric driving. The first peak occurs at a similar time to that of our PAD09 simulation.

The peak free magnetic energy built up before the first release is 1.45×10^{25} erg and 1.29×10^{25} erg for the PAD09 and PAD10 simulations, respectively. The energy buildup is greater in PAD09, as changes in connectivity do not occur until after the onset of the kink and the breaking of the structure's symmetry. In PAD10, the symmetry is already broken in the initial setup, so changes in connectivity can occur as soon as the simulation begins and magnetic energy can already be released.

Figure 5(a) shows $|j|/|B|$ in the *xz*-plane at $y = 9$ Mm for PAD09 (left), PAD10 (center), and PAD09R (right). An

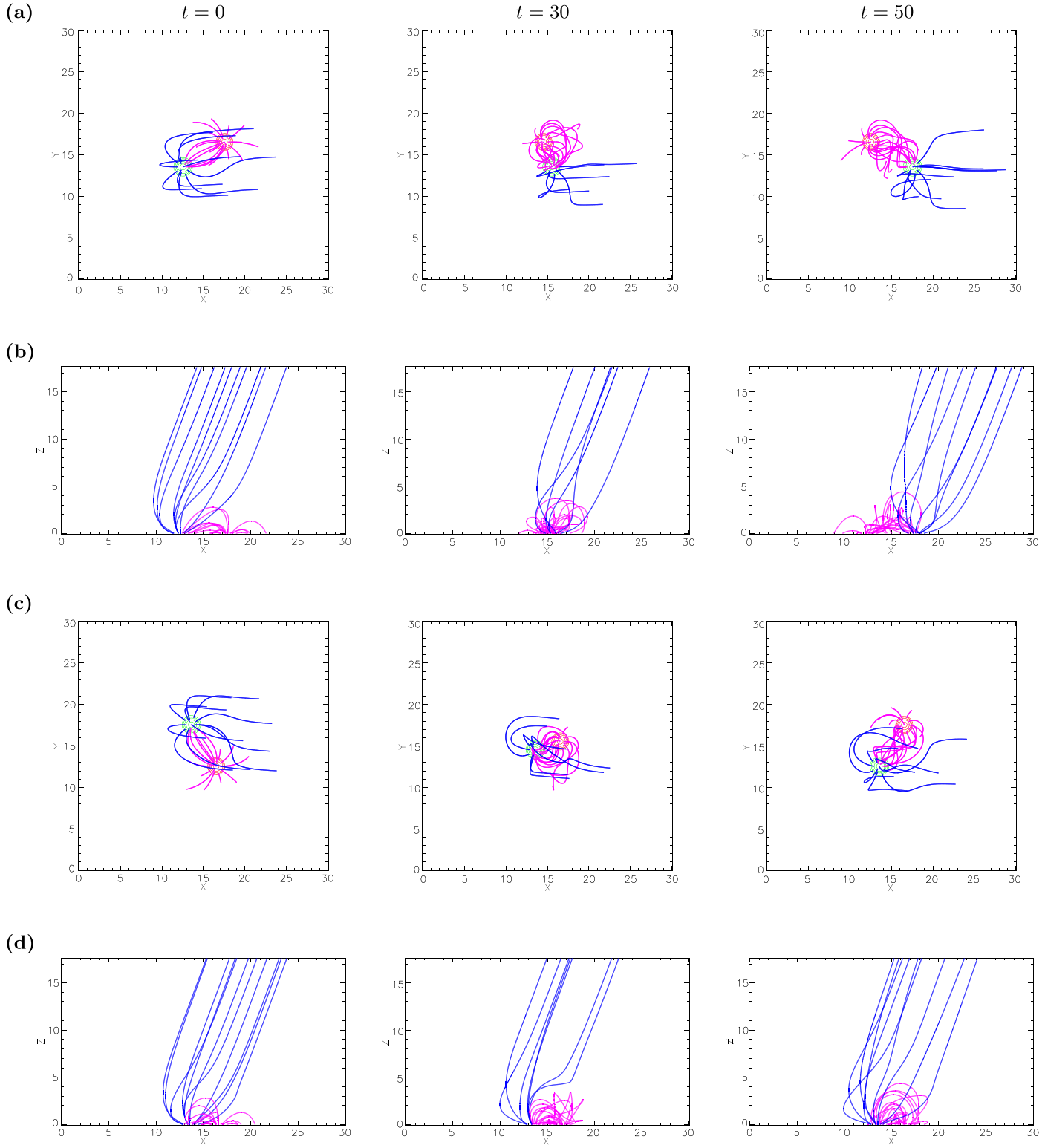

Figure 7. FLYBY1 ((a) and (b)) and FLYBY2 ((c) and (d)): closed (magenta) and open (blue) magnetic field lines viewed in the *xy*-plane ((a) and (c)) and *xz*-plane ((b) and (d)) at $t = 0$ (left), $t = 30$ (center) and $t = 50$ (right) time steps. An animation of the magnetic field lines viewed in the *xy*-plane for FLYBY1 (left panel) and FLYBY2 (right panel) running from time step 0 to 50 is provided online.

(An animation of this figure is available.)

animated version of these panels is available online. In PAD09 and PAD09R, current is initially all contained within the twisted dome of the jet and along the narrow, vertical jet spire, indicating that no twist has been released and almost all non-potentiality is contained within the dome. After the onset of the kink, the symmetry of the system is broken and we see a broader jet spire, as in Figure 5(a). In PAD10, the spire broadens more rapidly, as connectivity changes occur with

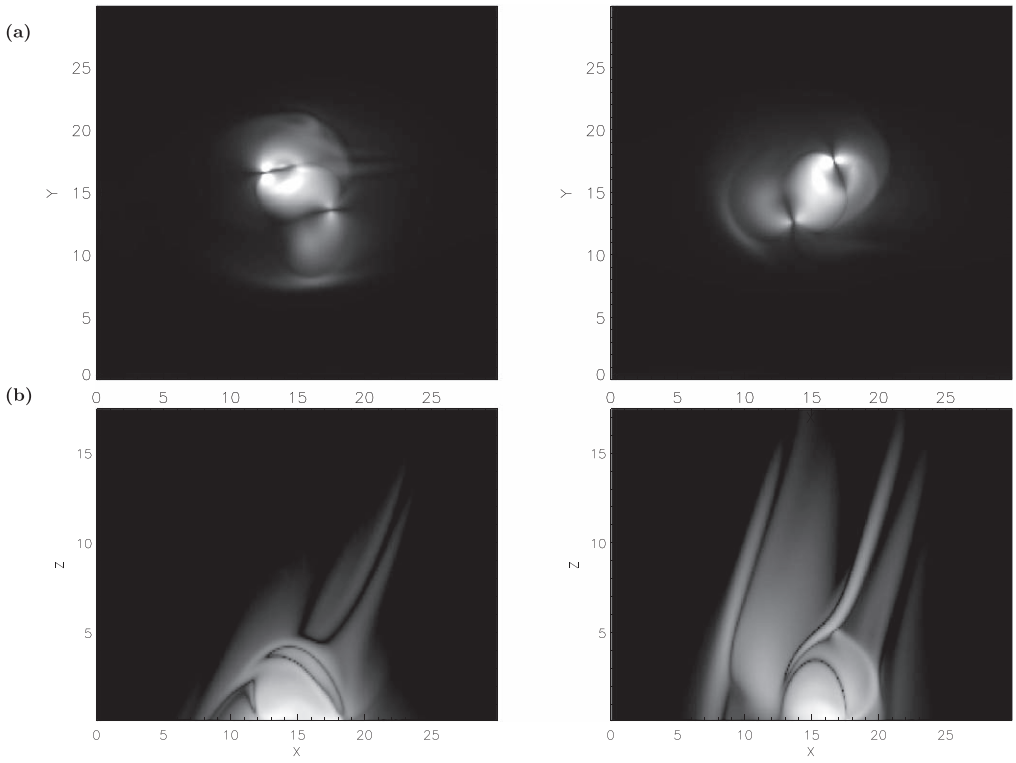

Figure 8. FLYBY1 (left) and FLYBY2 (right): (a) LOS-integrated current in the *xy*- plane and (b) logarithm of current in the *xz*-plane at $y = 15$ Mm, at $t = 50$ time steps. An animation of the LOS-integrated current in the *xy*-plane for FLYBY1 (left panel) and FLYBY2 (right panel) running from time step 0 to 50 is provided online.

(An animation of this figure is available.)

background magnetic field right from the start of the simulation, releasing some twist. The spire becomes broader as we see the dome of the jet begin to tip over, allowing more changes in connectivity. In a model that included more dynamics, such as the MHD model of Pariat et al. (2010), this would allow for fast reconnection and the rapid release of energy to occur, simulating a coronal jet.

Figure 5(b) shows the *xy* path of the magnetic null point from $t = 0$ to $t = 200$ time steps for PAD09 (left), PAD10 (center), and PAD09R (right). The path's color ranges from black/purple/blue near the start of each simulation, to red at $t = 200$. For PAD09 and PAD09R, the center point of the path shows up as blue because the null does not move from its initial position for the first 50 time steps (hence blue is plotted over black and purple). In contrast, the PAD10 null begins to move in a spiral from the start. In PAD09 and PAD10, the photospheric driving is constant throughout the simulations, continually injecting energy and twist, so that their null paths spiral outward. In PAD09R, the null begins to spiral back inward after the driving has stopped and the kink has occurred, as the system relaxes back toward an axisymmetric configuration and the spire begins to straighten.

3.2. CIRC

Figures 6(a) and (b) show field line plots in the *xz*-plane for the circular motion case, at $t = 30$ and $t = 120$ time steps (0.6 and 2.4 rotations, respectively); the evolution can be seen in an online animation. The circular motion causes the jet spire and surrounding background field lines to become twisted. It also allows for the release of magnetic energy, as can be seen in Figure 6(c). The black line displays the free magnetic energy throughout the simulation, and shows peaks before the completion of each circle. The null height (red line) shows a similar but mirrored evolution, with peaks occurring during troughs in the free energy. The free energy curve shows that energy is built up and decreases constantly in a smooth fashion. This is caused by compression and decompression of the magnetic field under the null dome, as the magnetic feature moves around the central axis. While energy is built up, twist is also built up within the jet dome, causing it to swell and push the null point upward. When the null point height is at its maximum, the free energy curve shows the sharpest decrease. The behavior of the free energy and null point height curves is similar to the case of Pariat et al. (2010).

As in PAD10, the changing connectivity and twisting of the background field results in a wider spire shape, which can be seen in the logarithm of current density (Figure 6(d) and the online animation). The offset rotation in our case appears to be enough to break the symmetry as in Pariat et al. (2010), allowing connectivity to change continually.

3.3. Flyby, Emergence, and Cancellation

Flyby (two magnetic elements shearing past one another), emergence, and cancellation are all common and widespread occurrences within the Sun's small-scale photospheric magnetic field (e.g., Galsgaard et al. 2000; Thornton & Parnell 2011; Iida et al. 2012; Lamb et al. 2013).

Figure 7 shows field line images from the two flyby simulations, in the *xy*- and *xz*-planes. Their evolution can also be seen in the online animated figure. In FLYBY1 (top) the direction of motion of the magnetic features is parallel/anti-parallel to the slope of the 10° inclined background magnetic

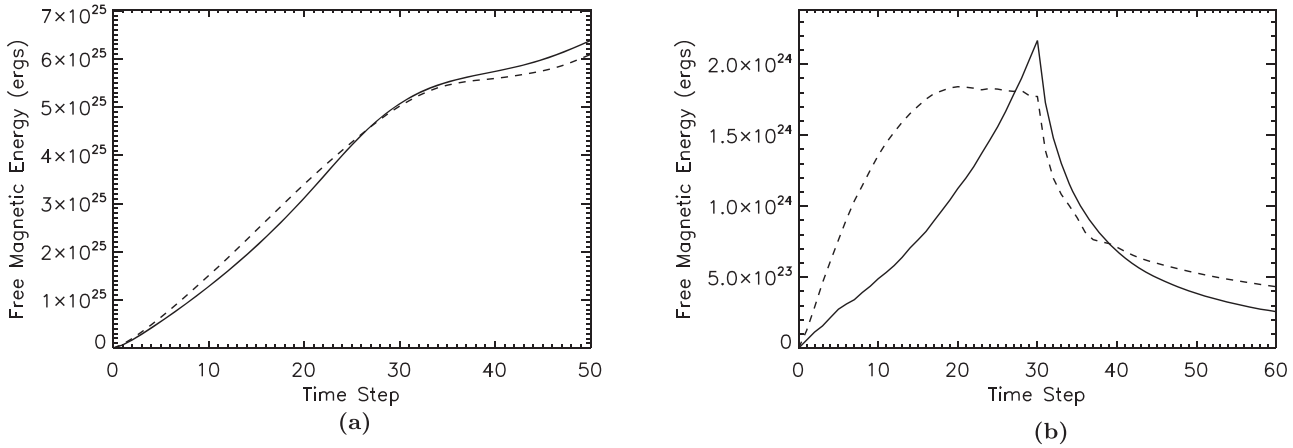

Figure 9. Free magnetic energy as a function of time for (a) the FLYBY1 (solid line) and FLYBY2 (dashed line); and (b) EMERGE (solid line) and CANCEL (dashed line) simulations.

field; in FLYBY2 (bottom) the motion of the magnetic features is perpendicular to the inclination of the background field. As the two magnetic features move past one another, field lines become twisted and sheared, forming a flux rope. In images of the LOS-integrated current (Figure 8(a)) this can be seen as a rough S-shape in the *xy*-plane. When viewed side-on in the *xz*-plane (Figure 8(b)), the current forms a broad, filamentary structure, such as may be observed of a blowout jet (e.g., Moore et al. 2010). Blowout jets have also been connected with the observation of microsigmoids; Raouafi et al. (2010, 2012) suggested that these S-shaped bright points could be the "progenitors of coronal jets." An animation of the LOS-integrated current in the *xy*-plane can be seen in the online version of Figure 8. A future study will consider and compare observations and models of microsigmoids.

Figure 9(a) shows the free magnetic energy as a function of time for FLYBY1 (solid line) and FLYBY2 (dashed line). The curve is very similar in both cases, with the greatest increase occurring as the magnetic features move toward and shear past one another, then increasing less rapidly as they separate.

Figure 10 shows *xz*-plane images for the emergence and cancellation simulations. In both simulations, the opposite polarity features move toward or away from each other along an axis that is aligned with the slope of the 10° inclined background magnetic field. The magnetofrictional technique cannot emerge twist or model plasma dynamics as in Moreno-Insertis et al. (2008), Moreno-Insertis & Galsgaard (2013), and Archontis & Hood (2013). The result is that the structure of the model is closer to that of a "standard jet" structure. Figure 10 (left) shows field line images for the (a) emergence and (b) cancellation, at $t = 25$ time steps. The right images show the logarithm of current density integrated along the LOS at the same time. At this time in the emergence simulation, the magnetic features have almost reached their full separation of 3 Mm. In the cancellation simulation, the magnetic features have almost fully canceled at the midpoint of the box. The evolution can be seen in the *xz*-plane in the animated Figure 10 online. As no shearing takes place to create twist, and no twist is injected into either simulation, in both cases the magnetic field quickly relaxes back toward a near potential state after the magnetic features have stopped moving. This can be seen in the plot of free magnetic energy, Figure 9(b), for the emergence (solid line) and cancellation (dashed line). The free energy rapidly increases from the start of the simulation until the photospheric magnetic field stops evolving at $t = 30$ time steps, then rapidly decreases. The end values of free energy in each case are at 12% of their peak value for emergence and 24% of their peak value for cancellation. The amount of free magnetic energy built up in the emergence and cancellation simulations is also significantly less than that in either of the flyby simulations. We compare all four simulations at $t = 30$ time steps, as the photospheric driving stops after this point in the emergence and cancellation cases. At this time, the values of free energy are 2.1×10^{24} erg and 1.8×10^{24} erg for emergence and cancellation, compared to 5.1×10^{25} erg and 5.0×10^{25} erg for the two flyby simulations. The shearing and twisting in the flyby cases builds up and stores significantly more free energy than the relatively simple emergence and cancellation events simulated here.

3.4. Discussion

For the cases discussed above, a variety of similar simulations were run, varying a number of different parameters to determine their effects. The parameters varied were the strength and angle of the background magnetic field, number of relaxation steps between frames, grid resolution, and the inclusion of diffusion or fourth-order hyperdiffusion (e.g., van Ballegooijen & Cranmer 2008). The effects on the simulations were not significant; the total amount of free magnetic energy and the expansion of the dome were slightly different, but the general evolution remained the same. A background magnetic field of non-uniform strength also did not have a significant effect on the results. For example, in the PAD10 simulation, including η_j diffusion of $0.01\frac{(\Delta x)^2}{\Delta t}$ results in an order of magnitude less free magnetic energy being built up and much less expansion of the dome (e.g., the increase in height of the null is only around 1 Mm, compared to around 6 Mm in Figure 3(c)). When hyperdiffusion of $\eta_4 = 0.001\frac{(\Delta x)^4}{\Delta t}$ or $\eta_4 = 0.005\frac{(\Delta x)^4}{\Delta t}$ is included (see, e.g., Meyer et al. 2013), the total free energy built up is around 2% and 6% less than the PAD10 simulation, respectively, and the dome expansion is only slightly less than in PAD10. For the PAD09 case, we ran simulations with 128^3 and 512^3 for comparison with the 256^3 simulation. Increasing the resolution from 128^3 to 256^3 resulted in an increase of 21.5% in free magnetic energy and an increase of 5.1% in the height of the null (greater expansion of the

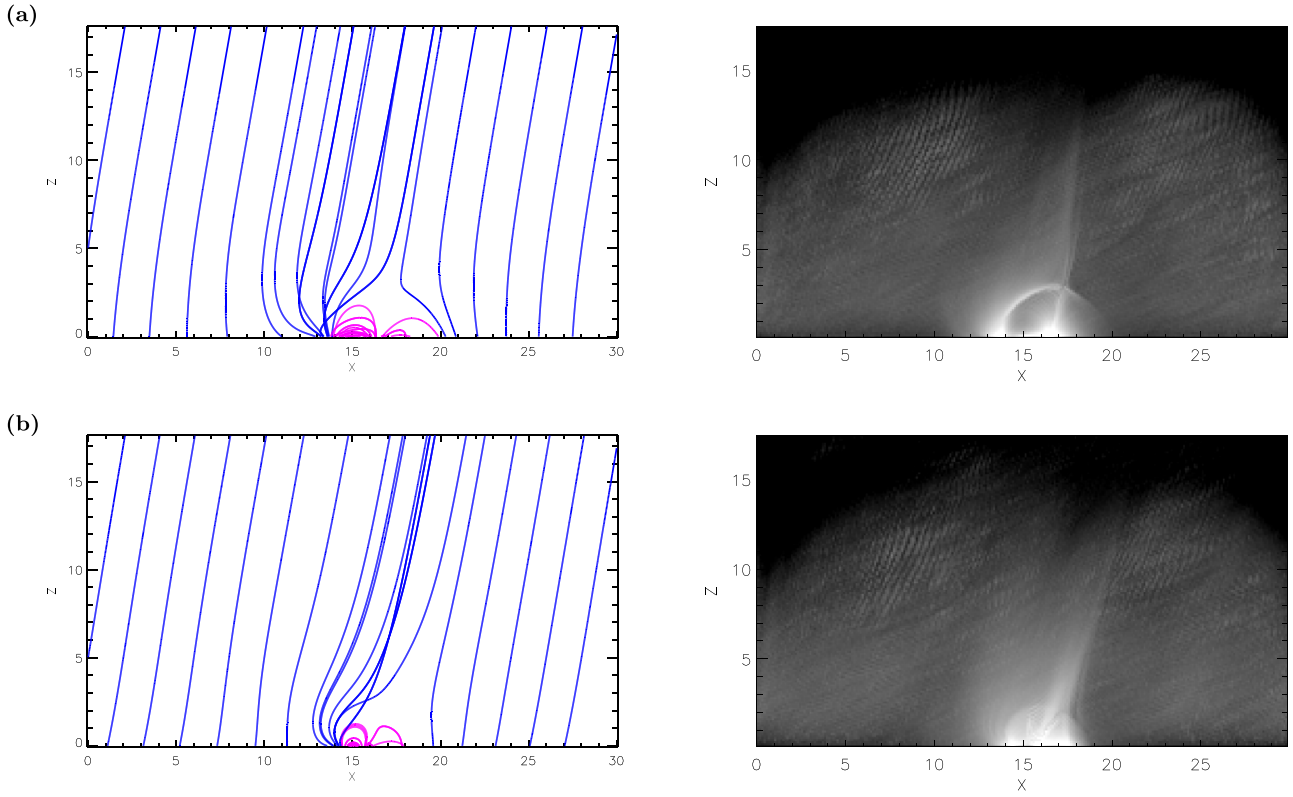

Figure 10. (a) Emergence and (b) cancellation images viewed in the *xz*-plane, at $t = 25$ time steps. Left: closed (magenta) and open (blue) magnetic field lines; right: logarithm of LOS-integrated current. An animation of this figure from time step 0 to 60 is provided online.

(An animation of this figure is available.)

Table 1
Summary of Results for Each Simulation (Refer to Figures for Temporal Evolution of Free Magnetic Energy)

Simulation	Peak Potential Field Energy ($\times 10^{26}$ erg)	Peak Free Magnetic Energy ($\times 10^{26}$ erg)	Flux of Positive Polarity ($\times 10^{17}$ Mx)	Visual Appearance
PAD09	2.2	0.15	3.0	Initially narrow spire, followed by broader spire after kink onset, twisted dome interior
and				
PAD09R		0.12		
PAD10	2.2	0.13	3.0	Wide spire, twisted dome interior
CIRC	10.7	0.025	3.0	Wide spire, flux rope
FLYBY1	8.7	0.64	9.4	Wide spire, flux rope
FLYBY2	8.7	0.61	9.4	Wide spire, flux rope
EMERGE	8.5	0.022	9.4	Narrow spire, no significant twist
CANCEL	8.5	0.018	9.4	Narrow spire, no significant twist

dome). Further increasing the resolution from 256^3 to 512^3 resulted in increases of 8.7% and 2.3% in the free magnetic energy and null height, respectively.

A summary of results is presented in Table 1, indicating the peak magnetic energy of the potential field and the free magnetic energy for each simulation, as well as the total flux of the positive polarity (for the flyby, emergence, and cancellation, the negative polarity has equal and opposite flux). Notice that in the PAD09, PAD10, and FLYBY setups we get a ratio of free energy to potential energy typical for standard solar flares (Savcheva & van Ballegooijen 2009; Savcheva et al. 2012) obtained from models with the magnetofrictional

technique, while in the rest of the configurations the ratio of free magnetic energy to potential energy is very small, suggesting that the boundary evolution in these cases either does not build a lot of non-potentiality or changing connectivity is more efficient at releasing it. This could be investigated further with an idealized MHD simulation. A brief description of the visual appearance of the jet structure is also given, and here we can make a qualitative comparison to the standard and blowout jet cartoons of Moore et al. (2010). Distinctions that Moore et al. (2010) suggest are that the blowout jet's magnetic field is significantly more twisted than that of a standard jet, with reconnection releasing twist along open field lines (e.g., Patsourakos et al. 2008), resulting in a broader jet spire. Often a cool component is observed as part of the jet, in what appears to be equivalent to a miniature filament eruption (Raouafi et al. 2010; Moore et al. 2013; Sterling et al. 2015). Archontis & Hood (2013) and Moreno-Insertis & Galsgaard (2013) present MHD simulations of blowout jets initiated via the emergence of a twisted magnetic flux rope. As discussed in the introduction, there have yet to be any conclusive observations of emergence as the triggering mechanism of a coronal jet.

Because no twist is injected into the emergence and cancellation simulations presented here, the result is that they build up the least amount of energy of the set, and a narrow jet spire is seen in the electric current images. These simulations are most reminiscent of the standard jet cartoon. The rotating (PAD09/10), circular motion (CIRC), and flyby (FLYBY1/2) simulations discussed above all result in significantly twisted magnetic field lines at the jet base, with the flyby simulations producing a clear sigmoidal structure in the resulting electric current. These simulations also produce a broad jet spire. In the MHD simulation of Pariat et al. (2009), reconnection occurs at the jet null point allowing for significant energy release and a helical jet spire. These simulations compare qualitatively to a blowout jet-type scenario. It will be interesting in the future to model the circular motion and flyby jet configurations in an MHD simulation, to compare the magnetic field evolution to the simulations discussed here, as well as consider the eruptive phase of the jet.

4. Conclusions and Future Work

We have presented eight different simulations to demonstrate the structure of solar coronal jets in largely unipolar regions. These involved rotation and circular motion of a single parasitic polarity; and flyby, emergence, and cancellation of two magnetic features of equal and opposite flux, all in a uniform background magnetic field. As the magnetofrictional technique used produces series of equilibria, it cannot accurately model the dynamic eruptive stage of the jet. Some change in connectivity or "reconnection" does happen due to numerical diffusion, although not to the same extent as in MHD, and this process depends on the parameters of magnetofriction, such as the ordinary and hyperdiffusion (not used in this case for simplicity). This "reconnection" is evidenced by the changes in the magnetic field configuration and topology over time and by the change in the magnetic free energy. We can, however, model the lead-up to the eruption; the building of magnetic energy and the formation of the jet structure. Savcheva et al. (2015, 2016) and Janvier et al. (2016) used a magnetofrictional relaxation technique to model an erupting unstable flux rope with "reconnection" beneath to reproduce a myriad of flare and CME features observed with AIA, *Hinode* and *STEREO*. So, the use of a relaxation technique in studying the lead-up to dynamical events has been tested against observations.

The presence of a vertical or slightly inclined background magnetic field within our simulations allows for the formation of the typical jet "spire" structure, as may be seen in a coronal hole, for example. More complex interactions between magnetic features, such as twisting and shearing, can lead to greater buildup of free magnetic energy and the formation of a flux rope. It is believed that small-scale microsigmoids could result in blowout type jets, perhaps a small-scale equivalent of a sigmoid leading to a coronal mass ejection (Raouafi et al. 2010). Indeed, Sterling et al. (2015) report miniature filament eruptions occurring in all of the jets they observe, suggesting that the same process occurs across a range of scales, from coronal mass ejections down to the smallest observed eruptions. In particular, the rotation, circular motion, and flyby simulations result in significant buildup of twist, electric current, and free magnetic energy.

Further studies will investigate the evolution of small-scale flux ropes related to jet-type events, and in particular produce simulations representing the theoretical standard and blowout jet cartoons as presented by Moore et al. (2010). In addition, we intend to run MHD simulations for comparison with specific cases from the present study (e.g., CIRC and FLYBY), for further validation of the magnetofrictional technique in this context. We will also compare the theoretical jet simulations here directly to observed case studies, as well as run magnetofrictional simulations of observed jet events driven by a sequence of HMI magnetograms as described in Gibb et al. (2014), which will be compared with observations from AIA and *IRIS*. We will investigate the kink simulations further to quantify the twist transferred in both magnetofrictional and MHD simulations using the new techniques described in Tassev & Savcheva (2019).

K.A.M. and D.H.M. gratefully acknowledge the support of the Leverhulme Trust, the STFC and the Carnegie Trust for the Universities of Scotland. K.A.M., A.S.S., and E.E.D. thank ISSI (Bern) for their support of the team "Understanding Solar Jets and their Role in Atmospheric Structure and Dynamics." D.H.M. thanks the EU for their support under FP7. Simulations were run using the STFC/SRIF funded UKMHD cluster at the University of St Andrews. A.A.S. and E.E.D.'s work on the project and K.A.M.'s visits to CfA were supported by NASA GI Grant #NNX15AF43G and NASA Focused Science Topic Grant #NNX11AO98G.

ORCID iDs

K. A. Meyer https://orcid.org/0000-0001-6046-2811
A. S. Savcheva https://orcid.org/0000-0002-5598-046X
D. H. Mackay https://orcid.org/0000-0001-6065-8531
E. E. DeLuca https://orcid.org/0000-0001-7416-2895

References

Adams, M., Sterling, A. C., Moore, R. L., & Gary, G. A. 2014, ApJ, 783, 11
Archontis, V., & Hood, A. W. 2008, ApJL, 674, 113
Archontis, V., & Hood, A. W. 2013, ApJL, 769, 21
Bout, M., Lamy, P., & Llebaria, A. 2002, ESA SP, 508, 379
Chen, H. D., Jiang, Y. C., & Ma, S. L. 2008, A&A, 478, 907
Cheung, M. C. M., De Pontieu, B., Tarbell, T. D., et al. 2015, ApJ, 801, 83
Cheung, M. C. M., & DeRosa, M. L. 2012, ApJ, 757, 147
Cirtain, J. W., Golub, L., Lundquist, L., et al. 2007, Sci, 318, 1580

Fang, F., Fan, Y., & McIntosh, S. W. 2014, ApJL, 789, 19
Galsgaard, K., Parnell, C. E., & Blaizot, J. 2000, A&A, 362, 395
Gibb, G. P. S., Mackay, D. H., Green, L. M., & Meyer, K. A. 2014, ApJ, 782, 71
Hong, J., Jiang, Y., Zheng, R., et al. 2011, ApJL, 738, 20
Iida, Y., Hagenaar, H. J., & Yokoyama, T. 2012, ApJ, 752, 149
Innes, D. E., Bučík, R., Guo, L. J., & Nitta, N. 2016, AN, 337, 1024
Janvier, M., Savcheva, A., Pariat, E., et al. 2016, A&A, 591, A141
Karpen, J. T., DeVore, C. R., Antiochos, S. K., & Pariat, E. 2017, ApJ, 834, 62
Lamb, D. A., Howard, T. A., DeForest, C. E., Parnell, C. E., & Welsch, B. T. 2013, ApJ, 774, 127
Mackay, D. H., Green, L. M., & van Ballegooijen, A. A. 2011, ApJ, 729, 97
Matsui, Y., Yokoyama, T., Kitagawa, N., & Imada, S. 2012, ApJ, 759, 15
Meyer, K. A., Mackay, D. H., & van Ballegooijen, A. A. 2012, SoPh, 278, 149
Meyer, K. A., Sabol, J., Mackay, D. H., & van Ballegooijen, A. A. 2013, ApJL, 770, 18
Moore, R. L., Cirtain, J. W., Sterling, A. C., & Falconer, D. A. 2010, ApJ, 720, 757
Moore, R. L., Sterling, A. C., Falconer, D. A., & Robe, D. 2013, ApJ, 769, 134
Moreno-Insertis, F., & Galsgaard, K. 2013, ApJ, 771, 20
Moreno-Insertis, F., Galsgaard, K., & Ugarte-Urra, I. 2008, ApJL, 673, 211
Morton, R. J., Verth, G., Fedun, V., Shelyag, S., & Erdélyi, R. 2013, ApJ, 768, 17
Nisticò, G., Bothmer, V., Patsourakos, S., & Zimbardo, G. 2009, SoPh, 259, 87
Panesar, N. K., Sterling, A. C., Moore, R. L., & Chakrapani, P. 2016, ApJL, 832, L7
Pariat, E., Antiochos, S. K., & DeVore, C. R. 2009, ApJ, 691, 61
Pariat, E., Antiochos, S. K., & DeVore, C. R. 2010, ApJ, 714, 1762
Pariat, E., Dalmasse, K., DeVore, C. R., Antiochos, S. K., & Karpen, J. T. 2015, A&A, 573, 130
Patsourakos, S., Pariat, E., Vourlidas, A., Antiochos, S. K., & Wuelser, J. P. 2008, ApJL, 680, 73
Rachmeler, L. A., Pariat, E., DeForest, C. E., Antiochos, S. K., & Török, T. 2010, ApJ, 715, 1556
Raouafi, N.-E., Bernasconi, P. N., Rust, D. M., & Georgoulis, M. K. 2012, in ASP Conf. Ser. 454, Hinode-3: The 3rd Hinode Science Meeting, ed. T. Sekii, T. Watanabe, & T. Sakurai (San Francisco, CA: ASP), 299
Raouafi, N.-E., Georgoulis, M. K., Rust, D. M., & Bernasconi, P. N. 2010, ApJ, 718, 981
Raouafi, N.-E., Patsourakos, S., Pariat, E., et al. 2016, SSRv, 201, 1
Sako, N. 2014, PhD thesis, The Graduate University for Advanced Studies
Sako, N., Shimojo, M., Watanabe, T., & Sekii, T. 2013, ApJ, 775, 22
Savcheva, A., Pariat, E., McKillop, S., et al. 2015, ApJ, 810, 96
Savcheva, A., Pariat, E., McKillop, S., et al. 2016, ApJ, 817, 43
Savcheva, A., & van Ballegooijen, A. 2009, ApJ, 703, 1766
Savcheva, A. S., Cirtain, J., DeLuca, E. E., et al. 2007, PASJ, 59, S771
Savcheva, A. S., Green, L. M., van Ballegooijen, A. A., & DeLuca, E. E. 2012, ApJ, 759, 105
Schrijver, C. J., Derosa, M. L., Metcalf, T. R., et al. 2006, SoPh, 235, 161
Shibata, K., Shimojo, M., Yokoyama, T., & Ohyama, M. 1996, ASPC, 111, 29
Shimojo, M., & Tsuneta, S. 2009, ApJ, 706, L145
Sterling, A. C., Moore, R. L., Falconer, D. A., & Adams, M. 2015, Natur, 523, 437
Szente, J., Toth, G., Manchester, W. B., IV, et al. 2017, ApJ, 834, 123
Tassev, S., & Savcheva, A. 2019, arXiv:1901.00865
Thornton, L. M., & Parnell, C. E. 2011, SoPh, 269, 13
Török, T., Aulanier, G., Schmieder, B., Reeves, K. K., & Golub, L. 2009, ApJ, 704, 485
Török, T., Lionello, R., Titov, V. S., et al. 2016, in ASP Conf. Ser. 504, Coimbra Solar Physics Meeting: Ground-based Solar Observations in the Space Instrumentation Era, ed. I. Dorotovic, C. Fischer, & M. Temmer (San Francisco, CA: ASP), 185
van Ballegooijen, A. A., & Cranmer, S. R. 2008, ApJ, 682, 644
van Ballegooijen, A. A., Priest, E. R., & Mackay, D. H. 2000, ApJ, 539, 983
Wang, Y.-M., Sheeley, N. R., Jr., & Socker, D. G. 1998, ApJ, 508, 899
Wedemeyer-Böhm, S., & Rouppe van der Voort, L. 2009, A&A, 507, L9
Wedemeyer-Böhm, S., Scullion, E., Steiner, O., et al. 2012, Natur, 486, 505
Yang, W. H., Sturrock, P. A., & Antiochos, S. K. 1986, ApJ, 309, 383
Young, P. R., & Muglach, K. 2014a, SoPh, 289, 3313
Young, P. R., & Muglach, K. 2014b, PASJ, 66, 12